Coseismic Coulomb Stress Changes on Intraplate Faults in the Western Quebec Seismic Zone, Canada: Implications for Seismic Hazards

Jeremy Rimando[1], Alexander L. Peace[1], Katsuichiro Goda[2], Navid Sirous[2], Philippe Rosset[3], Luc Chouinard[3]

[1]School of Earth, Environment & Society, McMaster University, 1280 Main Street W., Hamilton, ON, L8S 4K1, Canada
[2]Department of Earth Sciences, Western University, 1151 Richmond Street N., London, ON, N6A 5B7, Canada
[3]Department of Civil Engineering, McGill University, 817 Sherbrooke St W., Montreal, QC H3A 0C3, Canada

*Corresponding author: Jeremy Rimando
Email: rimandoj@mcmaster.ca

Abstract

There is currently no active fault map for the intraplate western Quebec seismic zone (WQSZ) in eastern Canada, and consequently, no detailed finite-fault source models which are critical for seismic hazard assessments in this region with a rapidly growing population. While previous numerical stress modelling studies have shown that mostly NNW-SSE to NW-SE-striking faults exhibit the highest potential for reactivation under the present-day tectonic stress field, such modelling is unable to take into account the interaction of faults and earthquakes. This study attempts to identify possible future rupture zones using Coulomb stress analysis. We explore the static stress transfer caused by select earthquakes (M_W > 4.5) in the past century to proximal 'receiver' faults in the WQSZ, with a focus on those that exhibit a relatively high reactivation potential, to identify faults that have been promoted to failure. The significance of Coulomb stress changes (ΔCFS) observed on the nearby 'receiver' faults varied widely. Among the events analyzed in this study, only the 1935 M_W 6.1 Témiscaming earthquake caused extensive positive Coulomb stress change (≥ 0.1 Bar) on its receiver fault. The modelled fault rupture extents suggest a range of earthquake magnitudes of M_W 6-7. This work is the first attempt to provide a physical basis for seismic hazard assessment input parameters in the WQSZ based on the results of numerical stress modelling.

1. Introduction

Identifying causative faults for the recorded seismicity in the intraplate western Quebec Seismic Zone (WQSZ) in eastern Canada, like in most intraplate settings worldwide, has proven to be challenging due to the paucity in contemporary surface-rupturing earthquakes and due to the poor preservation of the topographic expression of active deformation (**McCalpin, 2009; Stein, 2007**). While nodal planes of well-determined focal mechanisms for earthquakes in the WQSZ have been linked to candidate structures from the similarity in strike with nearby existing faults and lineaments, these interpretations remain speculative since definitive proof, in the form of surface rupture, has not been associated with any of the moderate-to strong earthquakes (between M_W 5 and M_W 6.1) in this region (e.g., **Bent 1996a, 1996b**). While large prehistoric earthquakes cannot be ruled out, geomorphic evidence for these is lacking. The poor preservation of surface ruptures is due in part to the long return periods for earthquakes in this stable continental region of the North American plate, which experiences on average approximately 3 earthquakes with a moment magnitude (M_W) > 5 every decade (**NRCan, 2023a**). This is in stark contrast with Western Canada, that has experienced > 100 earthquakes of M_W > 5 in less than 100 years, due to its location near the Cascadia subduction zone (**NRCan, 2023b**).

The seismicity in the WQSZ is attributed primarily to the reactivation of pre-existing structures (**Rimando and Peace, 2021**) under the contemporary tectonic stress field (**Mazzotti & Townend, 2010; Reiter et al., 2014; Snee & Zoback, 2020**). Previous regional numerical stress analyses (e.g., **Rimando and Peace, 2021**) have shown that the mainly reverse/thrust faulting on mostly NW-SE striking faults in the WQSZ, as indicated by earthquake focal mechanisms, is compatible with the present-day NE-SW maximum horizontal stress orientation (S_{Hmax}) that is associated with spreading along the Mid-Atlantic Ridge (**Richardson, 1992**). Structures that are currently being reactivated include faults and folds that are related to late Precambrian to early Paleozoic Iapetan rifting, and mechanical discontinuities related to Precambrian lithotectonic terranes and plate boundaries (**Culotta et al., 1990; Kumarapeli, 1978; Rimando, 1994; Rimando & Benn, 2005**). These structures, however, are associated with relict tectonic landforms that constitute most of the topographic relief in the WQSZ, such as the grabens and half-grabens of the NE-SW-striking Saint Lawrence rift system (SLRS), and the NE-SW-striking Ottawa-Bonnechere (OBG) and Timiskaming grabens (TG; Figure 1a) (**Kay, 1942; Lamontagne et al., 2020, and references therein; Lovell & Caine, 1970**).

Aside from the fact that earthquakes occur infrequently in the WQSZ, the glacial and deglacial history of the region may obscure or complicate the interpretation of any evidence of recent tectonic deformation. During the Late Wisconsinan deglaciation (~12 Ka), when most of the St. Lawrence was occupied by the Champlain Sea, it is likely that many single-event or cumulative deformation features may have been eroded or inundated (e.g., **Dyke et al., 2002**; **Parent and Occhietti, 2007**). Where evidence of recent deformation is present, there is currently a debate whether these are due to tectonic stress or glacio-isostatic adjustment, or both (e.g., **Adams, 1989; Brooks & Adams, 2020; Wallach et al., 1995**).

Although the instrumental records of seismicity indicate the occurrence of mostly low, and at most moderate-sized earthquakes in the WQSZ (**NRCan, 2023c**), the temporal coverage of seismicity records are too short to provide a reliable indication of the longer-term level of fault activity, including return periods and the potential for large magnitude earthquakes in the area. Globally, there is increasing evidence of large earthquakes occurring in many areas that have been previously appraised as “stable continental regions” (**Calais et al., 2016; Rimando et al., 2021**). The 1929 M_S 7.2 Grand Banks and the 1811–1812 M_W 7.2–8.2 New Madrid earthquakes, which occurred to the southwest and to the east of the WQSZ, respectively, are some examples of large earthquakes in eastern North America (**Bent, 1995; Hasegawa & Kanamori, 1987; Tuttle et al., 2002**). In the WQSZ itself, there is an abundance of off-fault paleoseismic evidence for possibly large magnitude earthquakes in the not-so-distant past, mostly from identification of seismites, such as subaqueous mass transport deposits and liquefaction features (**Aylsworth & Hunter, 2003; Brooks, 2013, 2014, 2015; Brooks & Adams, 2020**).

Unlike in the west coast of Canada, there is less seismic, geologic, and/or geodetic data on the nature, distribution, and extent of seismogenic structures in eastern Canada, as well as earthquake size estimates, that will allow the creation of fault-source-based probabilistic seismic hazard and risk analyses of individual faults (e.g., **Goda and Sharipov, 2021**) or seismic zones (e.g., **Halchuk et al., 2014**). Consequently, only areal source zone models based on historical seismicity are being utilized in the WQSZ to produce seismic hazard estimates for the National Building Code of Canada (NBCC; **Halchuk et al., 2014**). Current scenario-based seismic hazard and risk models in the WQSZ (e.g., **Ghofrani et al., 2015; Yu et al., 2016**), mainly use historical seismicity, and have yet to provide physical justification for the fault source’s characteristics (location, magnitudes, and kinematics) that these utilized.

While previous numerical stress simulations have narrowed down areas for further detailed analysis (**Rimando and Peace, 2021**), such as the long NW-SE-striking fault segments of relatively high slip tendency in the western and central portions of the WQSZ whose length would suggest a potential for high magnitude earthquakes (**Wells and Coppersmith, 1994**), such studies are unable to account for the interaction of faults and earthquakes (**Bott, 1959; Wallace, 1951**).

Coulomb stress analysis is a method that allows for the effects of static stress transfer due to earthquakes on nearby faults to be explored (**King et al., 1994**). Coulomb stress transfer studies have been previously used to identify possible future rupture zones in an effort to improve seismic disaster mitigation (e.g., **Parsons et al., 2008)**. Some studies immediately investigated the effects of single, recent large earthquakes on nearby faults (e.g., **Parsons et al., 2008; Li et al., 2021**), while some consider all the earthquakes in the historical record that are above an arbitrary magnitude threshold to systematically identify faults that have been promoted to failure (e.g., **Li et al., 2020**). Coulomb stress transfer studies have been carried out globally on earthquakes associated with different faulting styles in a variety of tectonic settings. Earthquake triggering on adjacent faults/fault segments by previous earthquakes has been demonstrated on well-studied fault systems associated with plate boundaries, such as the lithospheric-scale strike-slip San Andreas Fault in the USA (e.g., **Stein et al., 1992; King et al., 1994**) and the North Anatolian Fault in Turkey (e.g., **Stein et al., 1997**); the fold-and-thrust belts of Taiwan (e.g., **Chan and Stein, 2009**; **Lin et al. 2013**); subduction zone megathrusts (**Toda et al., 2011a**), and back-arc normal faults of Italy (e.g., **Walters et al., 2008**).

Coulomb stress analyses in intraplate settings are less common (e.g., **Mohammadi et al., 2019**), and while this method has been previously applied in the nearby Charlevoix Seismic Zone in Quebec (**Fereidoni and Atkinson, 2015**), it was done in the context of relating modern seismicity to a large historic earthquake in the 1600s and not with the goal of identifying possible future rupture zones. In this study, we analyze the Coulomb stress changes caused by seismicity in the past 100 years to nearby faults in the WQSZ with a focus on faults that exhibit a relatively high slip tendency (**Rimando and Peace, 2021**). The characteristics of faults that appear to be promoted to failure can provide input parameters for future seismic hazard and risk modeling, which may have implications for urban planning, seismic design, and managing industrial operations that could alter the stress states in the area.

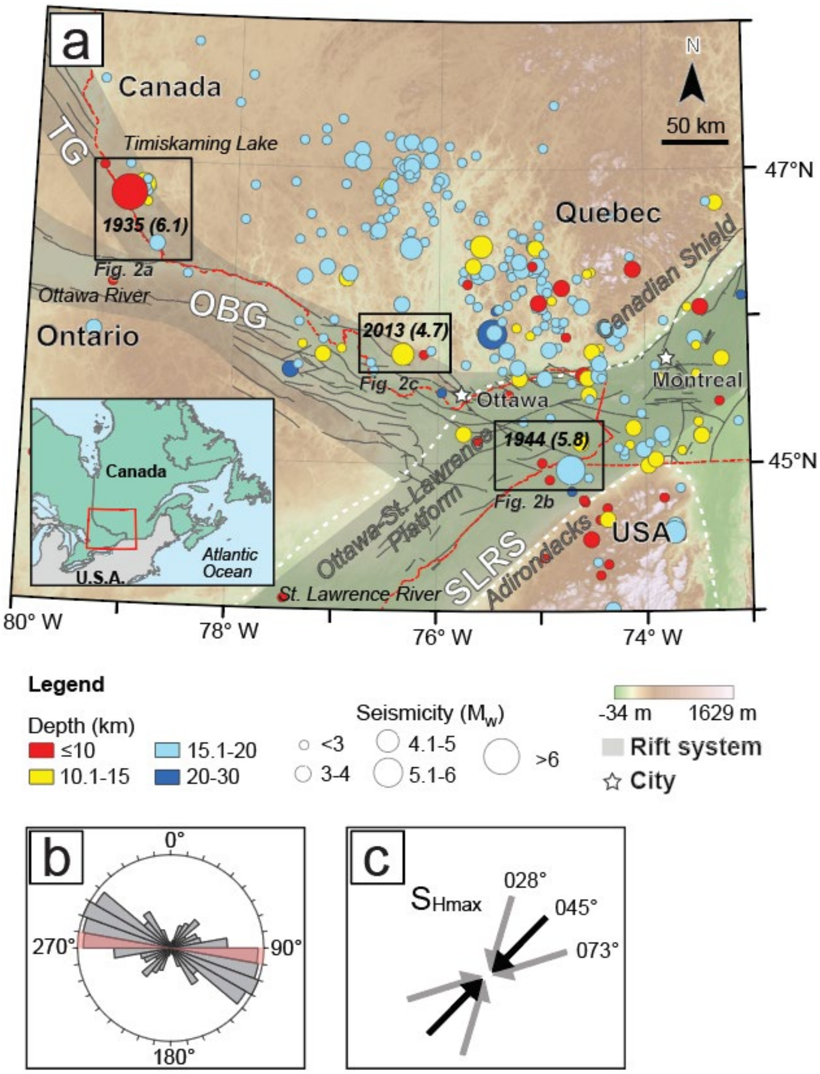

Figure 1. (**a**) Map of the major tectonic features, faults, and seismicity in the western Quebec seismic zone (WQSZ). TG—Timiskaming Graben. OBG—Ottawa-Bonnechere Graben. SLRS—Saint Lawrence Rift System. The white dashed line defines the borders of the different geological provinces: the Canadian Shield, the Ottawa-St. Lawrence Platform, and the Adirondacks. The red dashed line indicates the political boundaries. The inset map, at the bottom left, shows the location of the WQSZ in eastern North America. The earthquake epicenters are colored and scaled according to depth and magnitude, accordingly. The well-localized seismicity data was derived from Adams et al. (1988, 1989), Bent (1996a), Bent et al. (2002, 2003), Du et al. (2003), Horner et al. (1978), Ma and Eaton (2007), Seeber et al. (2002), Wahlström (1987), and the earthquake bulletins of both the Natural Resources Canada (NRCan, 2023c) and the United States Geological Survey (USGS, 2023). The base map is a 30-m-resolution Advanced Spaceborne Thermal Emission and Reflection Radiometer (ASTER) global digital elevation model (GDEM) by NASA JPL (2023) and the fault traces are from the Geological Survey of Canada's WQSZ faults map (Lamontagne et al., 2020). The black boxes indicate the locations of detailed maps (Figure 2) of areas with M_W > 4.5 events that were investigated in this study. (**b**) A rose diagram summarizing the orientations of the mapped faults in the WQSZ in 18 bins (10° intervals). (**c**) A diagram of the S_{Hmax} orientations in the WQSZ (Mazzotti & Townend, 2010); 045° is the average regional stress orientation, while 028° and 073° are the minimum and maximum values, respectively.

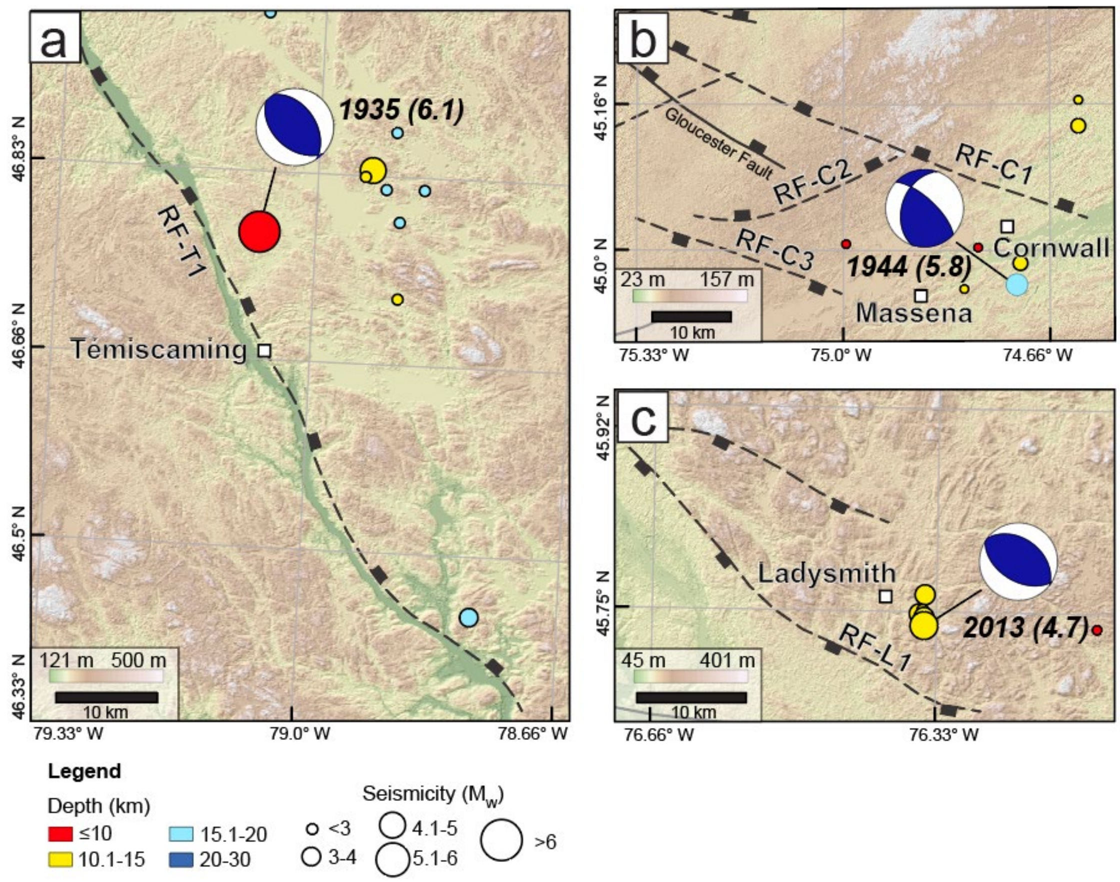

Figure 2. Locations of M_W > *4.5* earthquakes in the WQSZ. These maps show plots of the focal mechanisms of M_W > 4.5 earthquakes, background seismicity, and nearby mapped faults. **a**) The 1935 M_W 6.1 Témiscaming earthquake focal mechanism (Bent, 1996a) and receiver fault, RF-T1. **b**) The 1944 M_W 5.8 Cornwall-Massena earthquake focal mechanism (Bent, 1996b) and receiver faults, RF-C1, C2 & C3. **c**) The 2013 M_W 4.7 Ladysmith earthquake focal mechanism (Ma and Audet, 2014) and receiver fault, RF-L1. The topography is derived from a 30-m-resolution Advanced Spaceborne Thermal Emission and Reflection Radiometer global digital elevation models (ASTER GDEM) by NASA JPL (2023) and the fault traces are from the Geological Survey of Canada's WQSZ faults map (Lamontagne et al., 2020). Note that the pre-existing normal faults on this map are optimally oriented for reactivation as reverse faults (Rimando and Peace, 2021).

2. Methods and Data

We focused on instrumentally recorded M_W > 4.5 events in the WQSZ that are proximal to mapped faults to examine the stress perturbations that could potentially affect nearby faults.

A change in the Coulomb failure stress (ΔCFS), caused by coseismic slip on a fault (called *source fault*, which is not to be confused with finite-fault source models for seismic hazard assessments), can alter the state of stress in the surrounding rock volume. Positive and negative changes in the Coulomb failure stress (ΔCFS) on nearby faults (receiver faults), have been observed to promote and inhibit failure, respectively (**King et al., 1994**). ΔCFS is calculated using the following equation:

$$\Delta\mathrm{CFS} = \Delta\tau + \mu'\Delta\sigma_n,$$

where $\Delta\tau$ is the change in shear stress (which is positive in the direction of fault slip), $\Delta\sigma_n$ is the change in normal stress (which is positive if the fault is unclamped), and μ' is the apparent coefficient of friction.

We utilized the MATLAB-based software, Coulomb 3.4 (**Lin and Stein, 2004**; **Toda et al., 2005**), to model the coseismic static Coulomb stress changes on the receiver faults in an elastic half space (**Lin and Stein, 2004; Toda et al, 2005; Toda et al., 2011b**). While maps of coseismic surface fault ruptures, information on detailed 3D subsurface fault geometry, and models of finite-fault slip distributions were not available, we built realistically-scaled, planar source faults instead using information such as magnitude, strike, dip and rake from focal mechanisms for the 1935 M_W 6.1 Témiscaming (**Bent, 1996a**), 1944 M_W 5.8 Cornwall-Massena (**Bent, 1996b**), and 2013 M_W 4.7 Ladysmith (**Ma and Audet, 2014**) earthquakes. Receiver faults (RF-T1; RF-C1, C2 & C3; and RF-L1; **Figure 2**) were created by digitizing the faults and lineaments map compiled by the Geological Survey of Canada (Lamontagne et al., 2020). While the dip directions of these faults are known, dip values were not provided in the previous work. Thus, we assumed a dip of 60° (**Table 2**), which is corroborated by descriptions in previous studies of similar inherited, rift-related faults that abound the region (e.g., **Lovell & Caine, 1970**; **Rimando, 1994**; **Rocher & Tremblay, 2001**).

While most previous studies assign a default coefficient of friction (μ) value of either 0.4 when μ is unknown (e.g., **Stein, 1999**), or up to 0.8 for high-friction, low-cumulative-slip faults (**Lin and Stein, 2004**), we used a value of μ = 0.5, which is consistent with the value used in previous numerical stress modelling studies in the area (e.g., **Rimando and Peace, 2021**) that are based on sufficiently reliable geological justifications, such as the following: 1) the prevailing knowledge that mid-crustal maximum possible differential stress ($\sigma_1-\sigma_3$) values are most likely low in the region (e.g., **Hasegawa et al., 1985**; **Lamontagne & Ranalli, 1996**, and references therein), and 2) elevated levels of pore fluid pressure associated the upward migration of mantle-derived H_2O-CO_2-dominated fluids possibly enables the fault reactivation in eastern Canada (**Sibson, 1989**). A minimum ΔCFS threshold of 0.1 Bar has been shown to be sufficient to promote failure on nearby faults (**Stein, 1999**).

The scarcity of surface expressions, and consequently the lack of proper documentation of the kinematics of Quaternary active faults (e.g., **Brooks and Adams, 2020**), requires determining the kinematics of possible receiver fault through other means. To determine the kinematics, we calculated the expected kinematics (expressed in rake values; **Table 2**) of our receiver faults using the Java-based open-source software, Slicken 1.0 (**Xu et al., 2017**). Input for the calculations carried out in Slicken 1.0 included the following: 1) the dip angle and direction of the receiver fault; 2) the maximum horizontal stress directions, and 3) a stress ratio. Similar to the WQSZ fault slip tendency study by **Rimando and Peace (2021)**, we assumed stress states derived from inversions of distal earthquake focal mechanisms and borehole breakouts (**Mazzotti & Townend, 2010; Reiter et al., 2014; Snee & Zoback, 2020**), with an average S_{Hmax} = 045° and a stress ratio ($\phi = 1\text{-}R = \sigma_1 - \sigma_3 / \sigma_1 - \sigma_3$) of 0.4.

While we assumed specific values for the different input parameters in modelling Coulomb stress changes, we tested the sensitivity of our models to the range of usually assumed values for μ (minimum μ = 0.4 and maximum μ = 0.8), the range of modelled receiver fault rake values based on range of measured S_{Hmax} values in the WQSZ (minimum S_{Hmax} = 028° and maximum S_{Hmax} = 073°), and a range of feasible receiver fault dip values. Since there are no independent constraints to determine which of the two nodal planes of each of the double-couple focal mechanisms represents the ruptured fault plane of each event in consideration in this study, we consider both nodal planes as possible source faults for each earthquake (**Table 1**).

Date	**Magnitude (*Mw*)**	**Latitude (°N)**	**Longitude (°E)**	**Depth (km)**	**Nodal plane 1**			**Nodal plane 2**		
					Strike (°)	**Dip (°)**	**Rake (°)**	**Strike (°)**	**Dip (°)**	**Rake (°)**
Nov. 1, 1935	6.1	46.78	-79.07	10	130	45	80	324	46	100
Sept. 5,1944	5.8	44.96	-74.72	20	199	42	149	313	70	52
May 17, 2013	4.7	45.74	-76.35	14	306	41	94	122	50	87

Table 1. Source fault parameters (Data sources: Bent, 1996a; Bent, 1996b; Ma and Audet, 2014). Rake values (°) are reported following the convention of Aki and Richards (1980). Strike and dip values are reported following the right-hand rule.

Receiver Fault	**Strike (°)**	**Dip (°)**	**Rake (°)**
RF-T1	327	60	104
RF-C1	294	60	67
RF-C2	252	60	47
RF-C3	110	60	63
RF-L1	299	60	72

Table 2. Receiver fault parameters. Rake values (°) are reported following the convention of Aki and Richards (1980). Strike and dip values are reported following the right-hand rule.

3. Results

For each event, we displayed the calculated Coulomb stress changes in map view (horizontal slice at the focal depth), in cross-sectional view (across the source fault), and on the receiver fault plane itself. For each earthquake, we present the results of the 'preferred model,' which assumes a μ = 0.5 and a S_{Hmax} = 45°, and we present a sensitivity analysis, which consider a range of feasible μ, receiver fault rake (based on the assumed S_{Hmax}), and receiver fault dip values (**Figs. 3-5**).

3.1 The 1935 *M*$_W$ 6.1 Témiscaming Earthquake

3.1.1 Preferred model

The map view (10-km-depth slice) of Coulomb stress changes for both the SW- and NE-dipping source faults (**Figure 3a**&**d**, respectively; indicated as nodal planes 1 and 2, respectively in **Table 1**) of the 1935 *M*$_W$ 6.1 Témiscaming earthquake show that the NW end of the receiver fault (RF-T1) is affected the most by Coulomb stress changes, and that significant changes (≥ 0.1 Bar) occur close to the surface (0 km) and up to a depth of 30 km (**Figure 3b, c, e**&**f)**. Both maps exhibit roughly symmetric coulomb stress change patterns that are typical of dominantly reverse-slip, source-receiver fault pairs. The maps display ~40-km-long and ~15-to-20-km-wide NW-SE rectangular positive Coulomb stress change with central negative Coulomb stress change regions, which are spatially coincident with the map-view projections of the source faults. Both source fault model maps also show pairs of ~80-km-long (end-to-end) NE-SW lobes of negative Coulomb stress change (**Figure 3a**&**d**). In cross-sectional view (**Figure 3b**&**e**), radial patterns of positive and negative Coulomb stress changes can be seen, with the source faults almost entirely exhibiting negative Coulomb stress change, except at the tips, where lobes of positive stress changes emanate. In both cross-sections (**Figure 3b**&**e**), the central segment of the receiver fault (RF-T1) falls within a region of negative Coulomb stress change, while the upper and lower segments of the receiver fault (RF-T1) cross regions of positive Coulomb stress change. For both source fault models, the receiver fault plane (RF-T1, **Figure 3c**&**f**) exhibits a large extent of positive coulomb stress change: ~40-km-long, ~25-km-wide (downdip) doughnut-shaped regions that surround ~15-km-long and ~10-to-15-km-wide (downdip) central regions of negative Coulomb stress change, which correspond to the projections of the source fault planes.

3.1.2 Sensitivity Analysis

Overall, there is a minimal effect of changing the input values for μ and receiver fault rake on the Coulomb stress change distributions for both the SW- and NE-dipping source faults, as seen in map view, in cross-sectional view, and on the receiver fault (**Supplementary Figures S1-S6**).

In map view (**Supplementary Figures S1** & **S2**), a slight increase in the assumed coefficient of friction, such as between μ = 0.4 and μ = 0.5 has an insignificant effect on the stress change distributions. However, a larger increase in the coefficient of friction, such as between μ = 0.4 and μ = 0.8 appears to affect the stress change distributions more noticeably, with the Coulomb stress change distributions becoming more asymmetric, and the positive and negative regions increasing and decreasing in extent, respectively, as the coefficient of friction increases. As the receiver fault rake decreases (or as azimuth of the S_{Hmax} increases/S_{Hmax} is rotated clockwise), from 121° to 72° (S_{Hmax} = 028° to S_{Hmax} = 073°), the stress change patterns are rotated clockwise about an imaginary central vertical axis, which is most evident in the rotation of the lobes of negative Coulomb stress change, and the negative regions also decrease in extent.

In cross-sectional view (**Supplementary Figures S3** & **S4**), an increase in μ and S_{Hmax} azimuth, causes the stress patterns to bend/shear slightly towards the NE, and the positive (except for the lobe close to the lower portion of RF-T1) and negative regions to generally slightly increase and decrease in extent, respectively.

On the receiver fault plane (RF-T1, **Supplementary Figures S5** & **S6**), an increase in S_{Hmax} azimuth results in clockwise shearing of the Coulomb stress change patterns (and dilation of the 'slits' of positive Coulomb stress for the receiver fault of nodal plane 2 model). An increase in μ results in a slight increase in the negative Coulomb stress regions enveloping the positive Coulomb stress 'doughnut' pattern in both source fault models and changes the morphology of the central negative Coulomb stress patches – for the receiver fault of nodal plane 1 model, there's an increased indentation of the sides, while for the receiver fault of nodal plane 2 model, the 'slits' of positive Coulomb stress shrink.

Changing the assumed receiver fault dip for this event, however, yielded more noticeable changes in stress distributions for both source fault planes models (**Supplementary Figures S7** & **S8**). We tested the effect of the receiver fault dip only on the 1935 M_W 6.1 Témiscaming earthquake, as an event with a higher magnitude is likelier to be associated with more significant Coulomb stress changes. In map view, increasing the dip from 45° to 75° resulted in the counter-clockwise shearing of the stress patterns, with the stress pattern being significantly more asymmetric and exhibiting a more pronounced increase and decrease in positive and negative regions, respectively, for the model which assumes a dip of 75°. In cross-sectional view, an increase in dip causes the stress patterns to bend/shear slightly towards the NE, and the positive and negative regions to generally slightly increase and decrease, respectively, in extent, similar to the effect of changing the μ and S_{Hmax} azimuth. On the receiver fault plane, changing the receiver fault dip resulted in significantly different down-dip stress distributions. While the stress pattern changes didn't exhibit any obvious trend, a significant positive Coulomb stress patch which extended for at least ~ 5 km downdip was present in all receiver fault planes.

3.2 The 1944 M_W 5.8 Cornwall-Massena Earthquake

3.2.1 Preferred model

The stress changes in map view (20-km-depth slice) associated with NW- and NE-dipping source faults of the 1944 M_W 5.8 Cornwall-Massena earthquake (**Figure 4a&d**, respectively; indicated as nodal planes 1 and 2, respectively, in **Table 1**) appear to affect the SE end of the receiver fault (RF-C1). Both maps exhibit asymmetric coulomb stress change patterns that are typical of oblique reverse-slip, source-receiver fault pairs. The maps display ~50-km-wide sheared clover leaf-shaped distributions of positive Coulomb stress change, with irregularly-shaped centers and asymmetric paired lobes of negative Coulomb stress change (**Figure 4a&d**) owing to the large lateral-component of slip for both the source and receiver faults (**Table 1**).

Cross-sectional views (**Figure 4b&e**) of the two source fault models display different stress change patterns, with the NE-dipping source fault model having more defined radial patterns of positive and negative Coulomb stress changes as a result of the difference in the map-view stress change patterns between the two source fault models. Both cross-sections, however, exhibit a negative Coulomb stress change over most of the source faults and lobes of positive stress change at or near the tips.

The receiver fault planes for both source fault models (RF-C1, **Figure 4c&f**), shows insignificant Coulomb stress changes (-0.1 to 0.1 Bar) at the southeast end, with large (~20-km wide, 0-14 km downdip) negative Coulomb stress change patches, and smaller patches of positive coulomb stress at the lower SE corner of the receiver fault.

3.2.2 Sensitivity Analysis

There are noticeable, albeit minor effects as a result of changing the input values for μ and S_{Hmax} on the Coulomb stress change distributions for both the NW- and NE-dipping source faults (**Supplementary Figures S9-S14**).

In map view (**Supplementary Figures S9 & S10**), an increase in the assumed coefficient of friction from μ = 0.4 to μ = 0.8, results in an increase and decrease in the extent of the positive and negative regions, respectively. As the receiver fault rake decreases (or as azimuth of the S_{Hmax} increases/S_{Hmax} is rotated clockwise), from 85° to 48° (S_{Hmax} = 028° to S_{Hmax} = 073°), the lobes of negative Coulomb stress change become larger and distinct lobes of positive Coulomb stress change emerge.

In cross-sectional view (**Supplementary Figures S11 & S12**), an increase in μ results in a slight increase and decrease in the extent of the positive and negative regions, respectively, for both source models. An increase in the S_{Hmax} azimuth, causes the stress patterns to bend/shear slightly (towards the NW and the SW for the NW- and NE-dipping models, respectively), the positive regions to thin out, and the negative regions to decrease in extent, respectively.

On the receiver fault plane (RF-C1, **Supplementary Figures S13 & S14**), an increase in S_{Hmax} azimuth results in an increase and decrease in the extent and intensity of the negative and positive regions, respectively, for both source models. An increase in μ results causes as slight increase and decrease in the extent of the negative and positive regions, respectively, and an intensification of the negative stress regions.

We also modelled the Coulomb stress changes brought about by 1944 M_W 5.8 Cornwall-Massena earthquake on the other mapped faults surrounding the epicenter, RF-C2 and RF-C3 (**Supplementary Figures S15** & **S16**), but these yielded negligible Coulomb stress changes on the receiver fault, likely due to the greater distance of these faults from the hypocenter.

3.3 The 2013 M_W 4.7 Ladysmith Earthquake

3.3.1 Preferred model

The map view (14-km-depth slice) of Coulomb stress changes for both the NE- and SW-dipping source faults (**Figure 5a&d**, respectively; indicated as nodal planes 1 and 2, respectively in Table 1) of the 2013 M_W 4.7 Ladysmith earthquake show that the receiver fault (RF-L1) is unaffected. Both maps exhibit symmetric coulomb stress change patterns that are typical of dominantly reverse-slip, source-receiver fault pairs. The maps display ~8 to-10-km-wide positive Coulomb stress regions with central negative Coulomb stress change regions, which are roughly spatially coincident with the map-view projections of the source faults. Both source fault model maps also show pairs of ~10-to-12-km-long (end-to-end) NE-SW lobes of negative Coulomb stress change (**Figure 5a&d**).

In cross-sectional view (**Figure 5b&e**), radial patterns of positive and negative Coulomb stress changes that are at least ~5 km perpendicular distance to the receiver fault can be seen, with the source faults entirely exhibiting negative Coulomb stress change, and with lobes of positive stress changes emerging at or near the tips.

For both source fault models, the receiver fault plane (RF-L1, **Figure 5c&f**) does not exhibit any Coulomb stress changes.

3.3.2 Sensitivity Analysis

In general, there are only slight effects as a result of changing the input values for μ and S_{Hmax} on the Coulomb stress change distributions for both the NE- and SW-dipping source faults (**Supplementary Figures S17-S20**).

In map view (**Supplementary Figures S17 & S18**), an increase in the assumed coefficient of friction from μ = 0.4 to μ = 0.8, results in an increase and decrease in the extent of the positive and negative regions, respectively. As the receiver fault rake decreases (or as azimuth of the S_{Hmax} increases/S_{Hmax} is rotated clockwise), from 91° to

50° (S_{Hmax} = 028° to S_{Hmax} = 073°), the lobes of negative Coulomb stress change rotate and become larger.

In cross-sectional view (**Supplementary Figures S19 & S20**), an increase in μ tends to rotate the stress change patterns clockwise and make the larger positive and negative lobes slightly bigger and the smaller positive and negative lobes slightly smaller, for both source models. An increase in the S_{Hmax} azimuth, causes the entire stress patterns to decrease in size.

Regardless of the μ and S_{Hmax} values used, there was no observed Coulomb stress changes on the receiver fault plane (RF-L1).

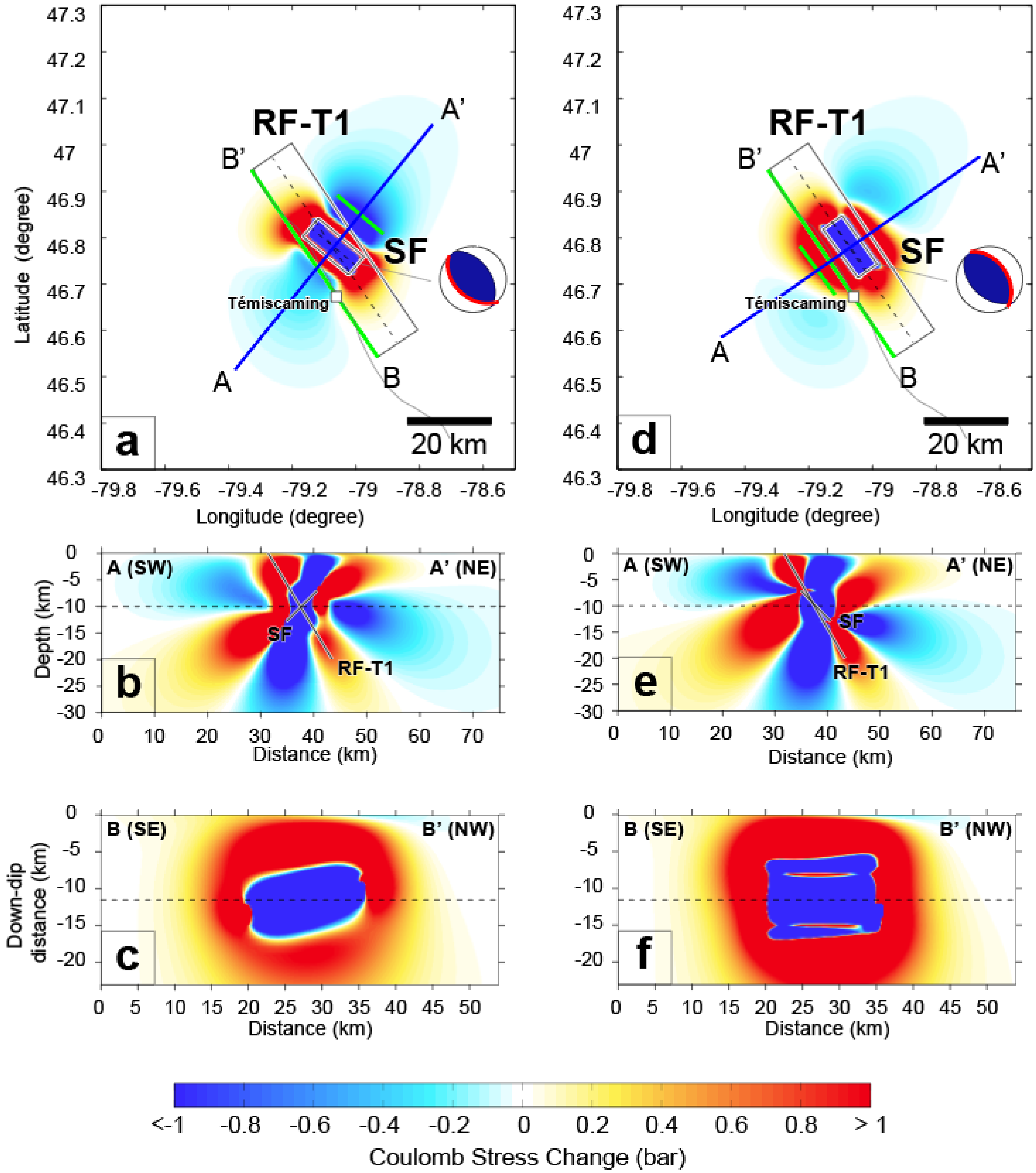

Figure 3. 1935 M_W 6.1 Témiscaming Earthquake Coulomb stress changes. Map-view (10-km depth slice) (**a&d**), cross-sectional view (**b&e**), and receiver fault plane view (**c&f**) of the Coulomb stress changes for the SW-dipping (**a- c**) and NE-dipping (**d-f**) source fault planes (nodal planes 1 and 2, respectively; Table 1). All calculations assumed a coefficient of friction (μ) of 0.5 and a receiver fault plane rake of 104°, based on a maximum horizontal stress value (SH_{max}) of 045°.

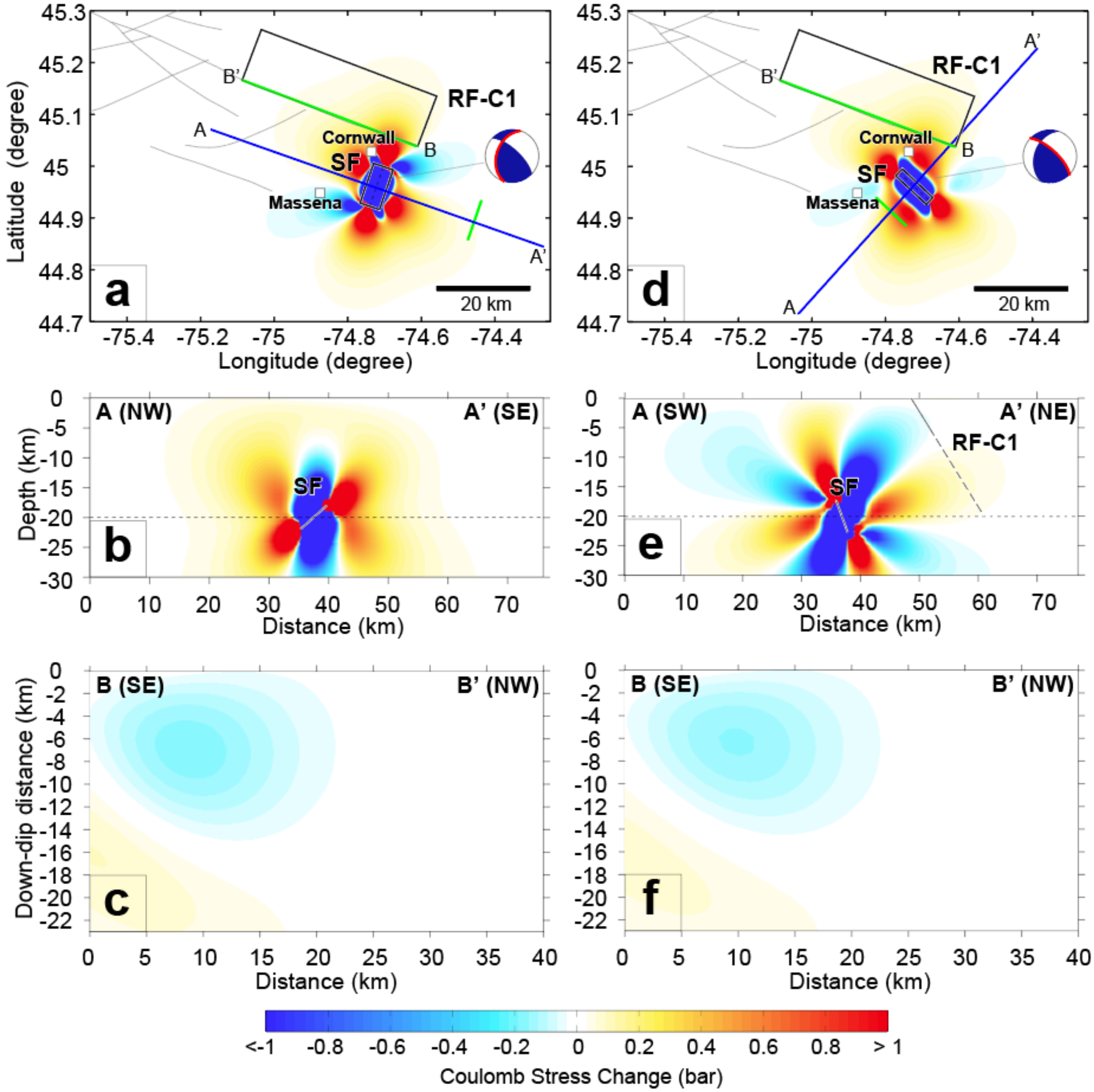

Figure 4. 1944 M_W 5.8 Cornwall-Massena Earthquake Coulomb stress changes. Map-view (20-km depth slice) (**a&d**), cross-sectional view (**b&e**), and receiver fault plane view (**c&f**) of the Coulomb stress changes for the NW-dipping (**a- c**) and NE-dipping (**d-f**) source fault planes (nodal planes 1 and 2, respectively; Table 1). All calculations assumed a coefficient of friction (μ) of 0.5 and a receiver fault plane rake of 67°, based on a maximum horizontal stress value (SH_{max}) of 045°.

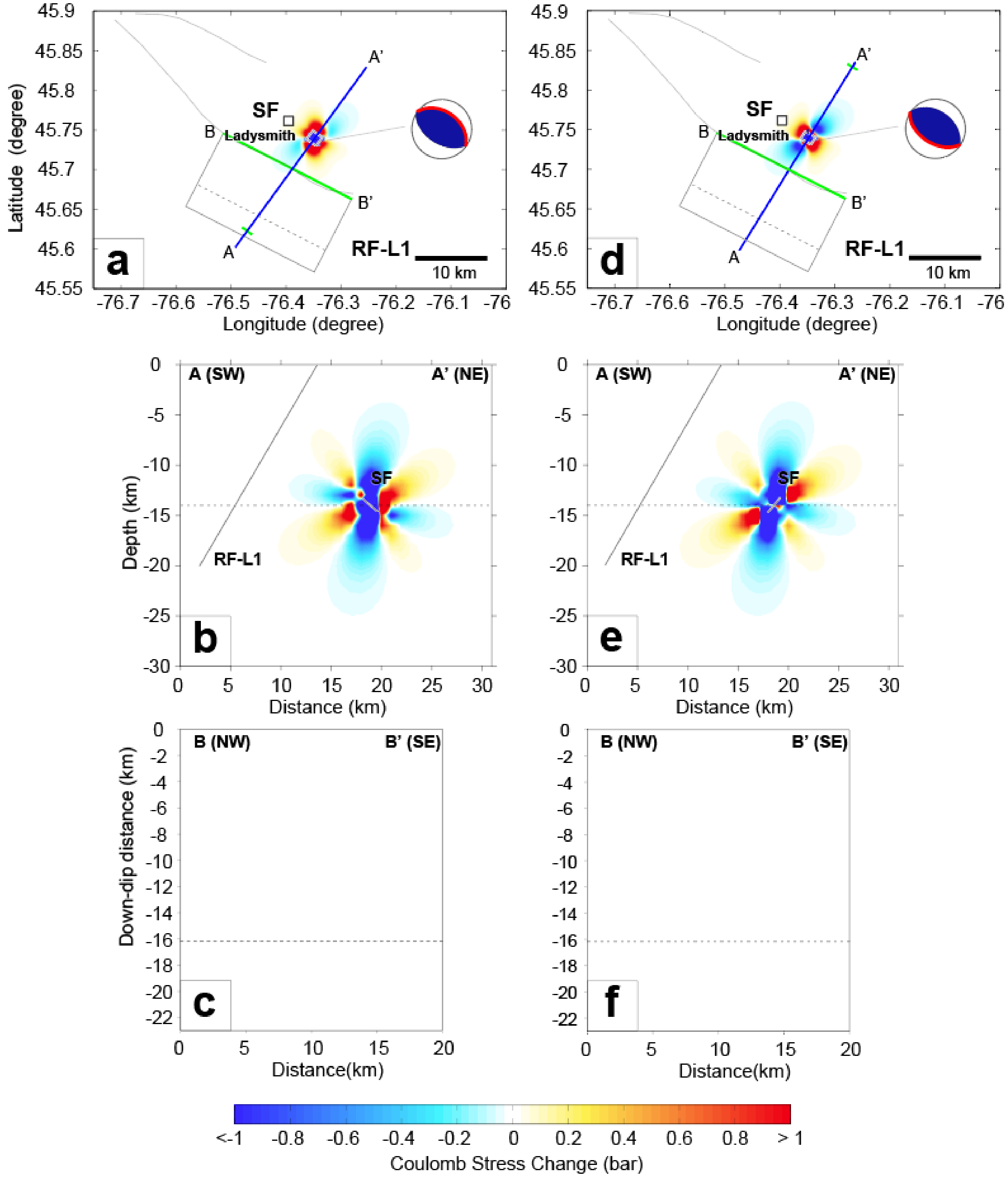

Figure 5. 2013 *Mw* 4.7 Ladysmith Earthquake Coulomb stress changes. Map-view (14-km depth slice) (**a&d**), cross-sectional view (**b&e**), and receiver fault plane view (**c&f**) of the Coulomb stress changes for the NE-dipping (**a- c**) and SW-dipping (**d-f**) source fault planes (nodal planes 1 and 2, respectively; Table 1). All calculations assumed a coefficient of friction (μ) of 0.5 and a receiver fault plane rake of 72°, based on a maximum horizontal stress value (SH_{max}) of 045°.

4. Discussion and Conclusions

Of the three events analyzed in this study, only the 1935 M_W 6.1 Témiscaming earthquake caused extensive positive (≥ 0.1 Bar) Coulomb stress change on a nearby mapped fault (receiver fault RF-T1, Figures 2 &3) owing to the proximity of the source and receiver faults, but more importantly to its relatively larger magnitude, as larger magnitude earthquakes redistribute tectonic stresses on faults over a much larger area (**Helmstetter et al., 2005**).

The positive Coulomb stress change (≥ 0.1 Bar) observed on the receiver fault, RF-T1, is extensive: ~40-km-long (end-to-end) and ~25-km-wide (downdip). However, at the center of this region of positive Coulomb stress is a patch of 15-km-long and ~10-to-15-km-wide (downdip) negative Coulomb stress change (**Figure 3**).

If we assume that the areal extent (km^2) of positive Coulomb stress change (≥ 0.1 Bar) on the receiver fault plane (RF-T1), which falls within the range of seismogenic depths of the WQSZ region, can be used to estimate the size (km^2) of future coseismic fault rupture (e.g., **Li et al., 2021**; **Shan et al., 2013**), then it is possible to estimate possible earthquake sizes (**Wells and Coppersmith, 1994**). Some of the many feasible rupture scenarios that can be drawn from the Coulomb stress pattern on the receiver fault, RF-T1 (**Figure 3c&f**), are as follows: 1) shallow rupture of entire positive Coulomb stress region (between ~7 km and ~47 km distance and 0-10 or 15 km downdip), 2) deeper rupture (between ~7 km and ~47 km distance and 10 -20 km downdip), 3) rupture of the entire positive Coulomb stress region (between ~7 km and ~47 km distance and 0-20 km depth), and 4) rupture of the entire downdip sections of either the SE end (~7 km and ~20 km distance) or NW end (~35 km and ~47 km distance) of the positive Coulomb stress region. The possible total fault rupture area of each of the aforementioned scenarios, or variations thereof, can further increase if rupture is also triggered on the patch of negative Coulomb stress. Therefore, fault rupture on parts, or the entire extent, defined by the positive Coulomb stress region on receiver fault RF-T1, could cause moderate-to-large earthquake moment magnitudes (M_W) ranging from ~6 to ~7 (**Wells and Coppersmith, 1994**).

The magnitude estimates based on the extent of positive coulomb stress changes on the receiver fault 'RF-T1' can provide parameters for future seismic hazard and risk modeling in the Témiscaming area. However, the potential for a significant earthquake in the Cornwall-Massena and Ladysmith areas cannot be entirely ruled out, as these are obviously seismically active areas, and since relatively high slip tendency values have also been measured on the NW-SE striking faults in these areas (**Rimando and Peace, 2021**).

While the population of Temiscaming is currently less than 3,000 (**Statistics Canada, 2017**), it is worth highlighting that rural Ontario is expecting to see a growth in population, due to the post-COVID-19 urban exodus (**Weeden, S., 2020**; **Wood, 2022**). Additionally, infrastructures in this area, like in most cities in eastern Canada are unlikely to be earthquake proof (**Goda, 2019; Kovacs, 2010; Mirza & Ali, 2017**). Improved knowledge of the level of seismic hazard in this area, from the earthquake magnitude estimates proposed in this study, could allow the following: 1) a better assessment of the suitability of the area for future urban development (e.g., **Bathrellos et al., 2017**); 2) proper implementation of seismic protection measures for timber structures (**Ugalde et al., 2019**) and historical structures and monuments (**Syrmakezis, 2006**); and 3) planning for mitigation of induced seismicity, potentially from industrial activity as the area develops.

While we used the best data that is currently available for the different input parameters, admittedly, modelling the Coulomb stress changes of the different > M_W 4.5 earthquakes in the WQSZ unavoidably incorporates epistemic uncertainties and some simplifying assumptions. One of the uncertainties pertains to the uncertainty in the magnitude, geometry, and kinematics and locations of source faults for the events that we analyzed. Despite using well-determined earthquake focal mechanisms (**Bent, 1996a, 1996b; Ma and Audet, 2014**) and accounting for the double-couple nature of these in our modelling, uncertainties that are inherent to seismic waveform inversions can also be caused by poor seismic station distribution and uncertainties in the hypothetical seismic velocity structure (e.g., **Lomax et al., 2009**; **Karasözen and Karasözen, 2020**). Since data on the detailed subsurface characteristics of the faults in consideration in this study are currently unavailable (e.g., from seismic reflection profiles), we used planar source and receiver fault models, from earthquake focal mechanisms and constant-dip projections of surface traces, respectively. The kinematics for both the source and receiver faults are also rather simplistic and/or hypothetical; for the source fault, in the absence of finite-fault slip models, we used rake values from earthquake focal mechanisms, and for the receiver faults, we used predicted rake values by imposing the regional stress field on the planar receiver faults.

As has been demonstrated in previous studies that analyzed the sensitivity of Coulomb stress changes to the different model input parameters (**Wang et al., 2014**), our sensitivity analysis shows that the coulomb stress distributions are most sensitive to the receiver fault dip angle (**Supplementary Figures S7 & S8**). As higher resolution input data becomes available in the future, accounting for these uncertainties in our current input data may result in deviations from the stress change patterns, intensity, and locations presented in this study. However, our analysis shows (**Supplementary Figures S7 & S8**) that for most conceivable and geologically realistic dip scenarios for the faults this region, the positive Coulomb stress change (≥ 0.1 Bar) distributions on the receiver fault of the 1935 M_W 6.1 Témiscaming earthquake, RF-T1, consistently cover an area of at least 30 km x 15 km, which is associated with a moment magnitude of M_W ≥ 6 (**Wells and Coppersmith, 1994**). Furthermore, the high slip tendency of NW-SE-striking faults in the WQSZ, corroborates our interpretation of the receiver fault 'RF-T1' as a potential future rupture zone.

Acknowledgements

Jeremy Rimando's postdoctoral fellowship at McMaster University was funded by the Natural Sciences and Engineering Research Council (NSERC)-Alliance grant (ALLRP 567023-21) in partnership with the Institute of Catastrophic Loss Reduction and in part by a Natural Sciences and Engineering Research Council NSERC Discovery Grant (RGPIN-2021-04011) awarded to Alexander Peace.

Availability Statement

The data that support the findings of this study are available in the Supporting Information and from the following references: Bent (1996a; https://doi.org/10.1007/BF00876667); Bent (1996b; https://doi.org/10.1785/BSSA0860020489); Ma and Audet (2014; https://doi.org/10.1139/cjes-2013-0215); and Lamontagne et al., (2020; https://doi.org/10.4095/321900). Version 3.4 of the Coulomb Software used for the Coulomb stress analysis in this study is available at https://www.usgs.gov/node/279387.

Other Information

The authors declare that they have no conflict of interest.

References

Adams, J., Sharp, J., & Stagg, M. C. (1988). New focal mechanisms for southeastern Canadian earthquakes (Geological Survey of Canada Open File Report 1992, p. 109). https://doi.org/10.4095/130428

Adams, J. (1989). Postglacial faulting in eastern Canada: Nature, origin and seismic hazard implications. Tectonophysics, 163(3–4), 323–331. https://doi.org/10.1016/0040-1951(89)90267-9

Adams, J., Vonk, A., Pittman, D., & Vatcher, H. (1989). New focal mechanisms for southeastern Canadian earthquakes (Geological Survey of Canada Open File Report 1995, Vol. II, p. 97). https://doi.org/10.4095/130594

Aki, K. and Richards P. G. (1980). Quantitative Seismology: Theory and Methods (Vol. 859). San Francisco, CA: Freeman.

Aylsworth, J. M., & Hunter, J. A. M. (2003). The Ottawa Valley Landslide Project: A geophysical and geotechnical investigation of geological controls on landsliding and deformation in Leda clay (pp. 227–234). Paper presented at the Third Canadian Conference on Geotechnique and Natural Hazards, GeoHazards.

Bathrellos, G. D., Skilodimou, H. D., Chousianitis, K., Youssef, A. M., & Pradhan, B. (2017). Suitability estimation for urban development using multi-hazard assessment map. Science of the total environment, 575, 119-134. https://doi.org/10.1016/j.scitotenv.2016.10.025

Bent, A. L. (1995). A complex double-couple source mechanism for the Ms 7.2 1929 Grand Banks earthquake. Bulletin of the Seismological Society of America, 85(4), 1003–1020. https://doi.org/10.1785/BSSA0850041003

Bent A. L. (1996a). An improved source mechanism for the 1935 Timiskaming, Quebec earthquake from regional waveforms, Pure Appl. Geophys. 146, no. 1, 5–20. https://doi.org/10.1007/BF00876667.

Bent A. L. (1996b). Source parameters of the damaging Cornwall-Massena earthquake of 1944 from regional waveforms, Bull. Seismol. Soc. Am. 86, no. 2, 489–497. https://doi.org/10.1785/BSSA0860020489

Bent, A. L., Drysdale, J., & Perry, H. C. (2003). Focal mechanisms for eastern Canadian earthquakes, 1994–2000. Seismological Research Letters, 74(4), 452–468. https://doi.org/10.1785/gssrl.74.4.452

Bent, A. L., Lamontagne, M., Adams, J., Woodgold, C. R., Halchuk, S., Drysdale, J., et al. (2002). The Kipawa, Quebec "Millennium" earthquake. Seismological Research Letters, 73(2), 285–297. https://doi.org/10.1785/gssrl.73.2.285

Bott, M. H. P. (1959). The mechanics of oblique slip faulting. Geological Magazine, 96(2), 109–117. https://doi.org/10.1017/S0016756800059987

Brooks, G. R. (2013). A massive sensitive clay landslide, Quyon Valley, southwestern Quebec, Canada, and evidence for a paleoearthquake triggering mechanism. Quaternary Research, 80(3), 425–434. https://doi.org/10.1016/j.yqres.2013.07.008

Brooks, G. R. (2014). Prehistoric sensitive clay landslides and paleoseismicity in the Ottawa valley, Canada. In Landslides in sensitive clays (Vol. 9, pp. 119–131). Springer. https://doi.org/10.1007/978-94-007-7079-9_10

Brooks, G. R. (2015). An integrated stratigraphic approach to investigating evidence of paleoearthquakes in lake deposits of Eastern Canada. Geoscience Canada, 42(2), 247. https://doi.org/10.12789/geocanj.2014.41.063

Brooks, G. R., & Adams, J. (2020). A review of evidence of glacially-induced faulting and seismic shaking in eastern Canada. Quaternary Science Reviews, 228, 106070. https://doi.org/10.1016/j.quascirev.2019.106070

Calais, E., Camelbeeck, T., Stein, S., Liu, M., & Craig, T. J. (2016). A new paradigm for large earthquakes in stable continental plate interiors. Geophysical Research Letters, 43(20), 10621–10637. https://doi.org/10.1002/2016GL070815

Chan, C. H., & Stein, R. S. (2009). Stress evolution following the 1999 Chi-Chi, Taiwan, earthquake: consequences for afterslip, relaxation, aftershocks and departures from Omori decay. Geophysical Journal International, 177(1), 179-192. https://doi.org/10.1111/j.1365-246X.2008.04069.x

Culotta, R. C., Pratt, T., & Oliver, J. (1990). A tale of two sutures: COCORP's deep seismic surveys of the Grenville province in the eastern US midcontinent. Geology, 18(7), 646–649. https://doi.org/10.1130/0091-7613(1990)018<0646:atotsc>2.3.co;2

Du, W. X., Kim, W. Y., & Sykes, L. R. (2003). Earthquake source parameters and state of stress for the northeastern United States and southeastern Canada from analysis of regional seismograms. Bulletin of the Seismological Society of America, 93(4), 1633–1648. https://doi.org/10.1785/0120020217

Dyke, A. S., Andrews, J. T., Clark, P. U., England, J. H., Miller, G. H., Shaw, J., & Veillette, J. J. (2002). The Laurentide and Innuitian ice sheets during the last glacial maximum. Quaternary Science Reviews, 21(1–3), 9–31. https://doi.org/10.1016/S0277-3791(01)00095-6

Fereidoni, Azadeh, and Gail M. Atkinson. "Correlation between Coulomb stress changes imparted by historic earthquakes and current seismicity in Charlevoix seismic zone, eastern Canada." Seismological Research Letters 86.1 (2015): 272-284. https://doi.org/10.1785/0220140134

Ghofrani, H., Atkinson, G. M., Chouinard, L., Rosset, P., & Tiampo, K. F. (2015). Scenario shakemaps for Montreal. Canadian Journal of Civil Engineering, 42(7), 463-476. https://doi.org/10.1139/cjce-2014-0496

Goda, K. (2019). Nationwide earthquake risk model for wood-frame houses in Canada. Frontiers in Built Environment, 5, 128. https://doi.org/10.3389/fbuil.2019.00128

Goda, K., & Sharipov, A. (2021). Fault-source-based probabilistic seismic hazard and risk analysis for Victoria, British Columbia, Canada: A case of the Leech River Valley Fault and Devil's Mountain Fault system. Sustainability, 13(3), 1440. https://doi.org/10.3390/su13031440

Halchuk, S., Allen, T. I., Adams, J., & Rogers, G. C. (2014). Fifth generation seismic hazard model input files as proposed to produce values for the 2015 National Building Code of Canada. Geological Survey of Canada, Open File, 7576(18), 57-123. https://doi.org/10.4095/293907

Hasegawa, H. S., Adams, J., & Yamazaki, K. (1985). Upper crustal stresses and vertical stress migration in eastern Canada. Journal of Geophysical Research, 90(B5), 3637–3648. https://doi.org/10.1029/JB090iB05p03637

Hasegawa, H. S., & Kanamori, H. (1987). Source mechanism of the magnitude 7.2 Grand Banks earthquake of November 1929: Double couple or submarine landslide? Bulletin of the Seismological Society of America, 77(6), 1984–2004. https://doi.org/10.1785/BSSA0770061984

Helmstetter, A., Kagan, Y. Y., and Jackson, D. D. (2005). Importance of small earthquakes for stress transfers and earthquake triggering. J. Geophys. Res., 110, B05S08. https://doi.org/10.1029/2004JB003286

Horner, R. B., Stevens, A. E., Hasegawa, H. S., & Leblanc, G. (1978). Focal parameters of the July 12, 1975, Maniwaki, Québec, earthquake—An example of intraplate seismicity in eastern Canada. Bulletin of the Seismological Society of America, 68(3), 619–640. https://doi.org/10.1785/BSSA0680030619

Karasözen, E., & Karasözen, B. (2020). Earthquake location methods. GEM-International Journal on Geomathematics, 11(1), 1-28. https://doi.org/10.1007/s13137-020-00149-9

Kay, G. M. (1942). Ottawa-Bonnechere graben and Lake Ontario homocline. Bulletin of the Geological Society of America, 53(4), 585–646. https://doi.org/10.1130/GSAB-53-585

King, G. C., Stein, R. S., & Lin, J. (1994). Static stress changes and the triggering of earthquakes. Bulletin of the Seismological Society of America, 84(3), 935-953. https://doi.org/10.1785/BSSA0840030935

Kovacs, P. (2010). Reducing the risk of earthquake damage in Canada: Lessons from Haiti and Chile. Institute for Catastrophic Loss Reduction.

Retrieved from https://www.iclr.org/wp-content/uploads/PDFS/lessons-from-haiti-and-chile.pdf

Kumarapeli, P. S. (1978). The St. Lawrence paleo-rift system: A comparative study. In Tectonics and geophysics of continental rifts (pp.367–384). Springer. https://doi.org/10.1007/978-94-009-9806-3_29

Lamontagne, M., & Ranalli, G. (1996). Thermal and rheological constraints on the earthquake depth distribution in the Charlevoix, Canada, intraplate seismic zone. Tectonophysics, 257(1), 55–69. https://doi.org/10.1016/0040-1951(95)00120-4

Lamontagne, M., Brouillette, P., Grégoire, S., Bédard, M. P., & Bleeker, W. (2020). Faults and lineaments of the western Quebec seismic zone, Quebec and Ontario (Open File 8361, p. 28). Geological Survey of Canada. https://doi.org/10.4095/321900

Li, Y., Shao, Z., Shi, F., & Chen, L. (2020). Stress evolution on active faults in the southwestern Yunnan region, southeastern Tibetan Plateau, and implications for seismic hazard. Journal of Asian Earth Sciences, 200, 104470. https://doi.org/10.1016/j.jseaes.2020.104470

Li, Y., Huang, L., Ding, R., Yang, S., Liu, L., Zhang, S., & Liu, H. (2021). Coulomb stress changes associated with the M7. 3 Maduo earthquake and implications for seismic hazards. Natural Hazards Research, 1(2), 95-101. https://doi.org/10.1016/j.nhres.2021.06.003

Lin, J., & Stein, R. S. (2004). Stress triggering in thrust and subduction earthquakes and stress interaction between the southern San Andreas and nearby thrust and strike-slip faults. Journal of Geophysical Research, 109. https://doi.org/10.1029/2003JB002607

Lin, D. H., Chen, K. H., Rau, R. J., & Hu, J. C. (2013). The role of a hidden fault in stress triggering: Stress interactions within the 1935 Mw 7.1 Hsinchu–Taichung earthquake sequence in central Taiwan. Tectonophysics, 601, 37-52. https://doi.org/10.1016/j.tecto.2013.04.022

Lomax, A., Michelini, A., & Curtis, A. (2009). Earthquake location, direct, global-search methods. In R. A. Meyers (Ed.), Encyclopedia of Complexity and Systems Science (pp. 2449–2473). New York, NY: Springer New York. https://doi.org/10.1007/978-0-387-30440-3_150

Lovell, H. L., & Caine, T. W. (1970). Lake Temiskaming Rift Valley (Ontario Department of Mines Miscellaneous Paper 39, p. 16). Retrieved from http://www.geologyontario.mndm.gov.on.ca/mndmfiles/pub/data/records/MP039.html

Ma, S., & Eaton, D. W. (2007). Western Quebec seismic zone (Canada): Clustered, midcrustal seismicity along a Mesozoic hot spot track. Journal of Geophysical Research, 112(B6). https://doi.org/10.1029/2006JB004827

Ma, S., & Audet, P. (2014). The 5.2 magnitude earthquake near Ladysmith, Quebec, 17 May 2013: Implications for the seismotectonics of the Ottawa–Bonnechere Graben. Canadian Journal of Earth Sciences, 51(5), 439–451. https://doi.org/10.1139/cjes-2013-0215

Mazzotti, S., & Townend, J. (2010). State of stress in central and eastern North American seismic zones. Lithosphere, 2(2), 76–83. https://doi.org/10.1130/L65.1

McCalpin, J. P. (Ed.). (2009). Paleoseismology (2nd ed., p. 613, International Geophysics Series). Academic Press.

Mirza, S., & Ali, M. S. (2017). Infrastructure crisis—A proposed national infrastructure policy for Canada. Canadian Journal of Civil Engineering, 44(7), 539–548. https://doi.org/10.1139/cjce-2016-0468

Mohammadi, H., Quigley, M., Steacy, S., & Duffy, B. (2019). Effects of source model variations on Coulomb stress analyses of a multi-fault intraplate earthquake sequence. Tectonophysics, 766, 151-166. https://doi.org/10.1016/j.tecto.2019.06.007

NASA JPL (2023). Retrieved January 10, 2023, from https://asterweb.jpl.nasa.gov/

NRCan (2023a). Earthquake zones in Eastern Canada. Retrieved January 15, 2023, from https://earthquakescanada.nrcan.gc.ca/zones/eastcan-en.php#WQSZ

NRCan (2023b). Earthquake zones in Western Canada. Retrieved January 15, 2023, from https://earthquakescanada.nrcan.gc.ca/zones/westcan-en.php

NRCan (2023c). Earthquakes Canada. Retrieved January 15, 2023, from https://earthquakescanada.nrcan.gc.ca/index-en.php

Parent, M., & Occhietti, S. (2007). Late Wisconsinan deglaciation and Champlain Sea invasion in the St. Lawrence valley, Québec. Géographie physique et Quaternaire, 42(3), 215-246. https://doi.org/10.7202/032734ar

Parsons, T., Ji, C., & Kirby, E. (2008). Stress changes from the 2008 Wenchuan earthquake and increased hazard in the Sichuan basin. Nature, 454(7203), 509-510. https://doi.org/10.1038/nature07177

Reiter, K., Heidbach, O., Schmitt, D., Haug, K., Ziegler, M., & Moeck, I. (2014). A revised crustal stress orientation database for Canada. Tectonophysics, 636, 111–124. https://doi.org/10.1016/j.tecto.2014.08.006

Richardson, R. M. (1992). Ridge forces, absolute plate motions, and the intraplate stress field. Journal of Geophysical Research, 97(B8), 11739–11748. https://doi.org/10.1029/91JB00475

Rimando, R. E. (1994). Tectonic framework and relative ages of structures within the Ottawa–Bonnechère Graben (MSc thesis). University of Ottawa. Retrieved from https://ruor.uottawa.ca/handle/10393/10346

Rimando, R. E., & Benn, K. (2005). Evolution of faulting and paleo-stress field within the Ottawa graben, Canada. Journal of Geodynamics, 39(4), 337–360. https://doi.org/10.1016/j.jog.2005.01.003

Rimando, J. M., & Peace, A. L. (2021). Reactivation potential of intraplate faults in the western Quebec seismic zone, eastern Canada. Earth and Space Science, 8, e2021EA001825. https://doi.org/10.1029/2021EA001825

Rimando, J., Schoenbohm, L. M., Ortiz, G., Alvarado, P., Venerdini, A., Owen, L. A., et al. (2021). Late Quaternary intraplate deformation defined by the Las Chacras Fault Zone, West-Central Argentina. Tectonics, 40, e2020TC006509. https://doi.org/10.1029/2020TC006509

Rocher, M., & Tremblay, A. (2001). L'effondrement de la plate-forme du Saint-Laurent: Ouverture de Iapetus ou de l'Atlantique? Apport dela reconstitution des paléocontraintes dans la régionde Québec (Canada). Comptes Rendus de l'Académie des Sciences Paris, Sciences de la Terre et des planets, 333, 171–178. https://doi.org/10.1016/S1251-8050(01)01610-X

Seeber, L., Kim, W. Y., Armbruster, J. G., Du, W. X., Lerner-Lam, A., & Friberg, P. (2002). The 20 April 2002 Mw 5.0 earthquake near Au Sable Forks, Adirondacks, New York: A first glance at a new sequence. Seismological Research Letters, 73(4), 480–489. https://doi.org/10.1785/gssrl.73.4.480

Shan, B., Xiong, X., Wang, R., Zheng, Y., & Yang, S. (2013). Coulomb stress evolution along Xianshuihe–Xiaojiang Fault System since 1713 and its interaction with Wenchuan earthquake, May 12, 2008. Earth and Planetary Science Letters, 377, 199-210. https://doi.org/10.1016/j.epsl.2013.06.044

Sibson, R. H. (1989). High-angle reverse faulting in northern New Brunswick, Canada, and its implications for fluid pressure levels. Journal of Structural Geology, 11(7), 873–877. https://doi.org/10.1016/0191-8141(89)90104-1

Snee, J. E. L., & Zoback, M. D. (2020). Multiscale variations of the crustal stress field throughout North America. Nature Communications, 11(1), 1–9. https://doi.org/10.1038/s41467-020-15841-5

Statistics Canada (2017). Témiscaming, V [Census subdivision], Quebec and Quebec [Province] (table). Census Profile. 2016 Census. Statistics Canada Catalogue no. 98-316-X2016001. Ottawa. Retrieved February 10, 2023, from https://www12.statcan.gc.ca/census-recensement/2016/dp-pd/prof/index.cfm?Lang=E

Stein, R. S. (1999). The role of stress transfer in earthquake occurrence. Nature, 402(6762), 605-609. https://doi.org/10.1038/45144

Stein, S. (2007). Approaches to continental intraplate earthquake issues. In Continental intraplate earthquakes: Science, hazard, and policy issue (Vol. 425, pp. 1–16). Geological Society of American Spectrum Paper. https://doi.org/10.1130/2007.2425(01)

Stein, R. S., King, G. C. P., & Lin, J. (1992). Change in failure stress on the San Andreas and surrounding faults caused by the 1992 M= 7.4 Landers earthquake. Science, 258, 1328-1332. https://www.science.org/doi/abs/10.1126/science.258.5086.1328

Stein, R. S., Barka, A. A., & Dieterich, J. H. (1997). Progressive failure on the North Anatolian fault since 1939 by earthquake stress triggering. Geophysical Journal International, 128(3), 594-604. https://doi.org/10.1111/j.1365-246X.1997.tb05321.x

Syrmakezis, C. A. (2006). Seismic protection of historical structures and monuments. Structural Control and Health Monitoring: The Official Journal of the International

Association for Structural Control and Monitoring and of the European Association for the Control of Structures, 13(6), 958-979. https://doi.org/10.1002/stc.89

Toda, S., Stein, R. S., Richards-Dinger, K., & Bozkurt, S. B. (2005). Forecasting the evolution of seismicity in Southern California: Animations built on earthquake stress transfer. Journal of Geophysical Research,110, B05S16. https://doi.org/10.1029/2004JB003415

Toda, S., Lin, J., & Stein, R. S. (2011a). Using the 2011 Mw 9.0 off the Pacific coast of Tohoku Earthquake to test the Coulomb stress triggering hypothesis and to calculate faults brought closer to failure. Earth, Planets and Space, 63, 725-730. https://doi.org/10.5047/eps.2011.05.010

Toda, S., Stein, R. S., Sevilgen, V., & Lin, J. (2011b). Coulomb 3.3 Graphic-rich deformation and stress-change software for earthquake, tectonic, and volcano research and teaching—user guide. US Geological Survey open-file report, 1060(2011), 63.

Tuttle, M. P., Schweig, E. S., Sims, J. D., Lafferty, R. H., Wolf, L. W., & Haynes, M. L. (2002). The earthquake potential of the New Madrid seismic zone. Bulletin of the Seismological Society of America, 92(6), 2080–2089. https://doi.org/10.1785/0120010227

Ugalde, D., Almazán, J. L., Santa María, H., & Guindos, P. (2019). Seismic protection technologies for timber structures: a review. European journal of wood and wood products, 77, 173-194. https://doi.org/10.1007/s00107-019-01389-9

USGS (2023). Earthquakes. Retrieved January 15, 2023, from https://www.usgs.gov/natural-hazards/earthquake-hazards/earthquakes

Wahlström, R. (1987). Focal mechanisms of earthquakes in southern Quebec, southeastern Ontario, and northeastern New York with implications for regional seismotectonics and stress field characteristics. Bulletin of the Seismological Society of America, 77(3), 891–924. https://doi.org/10.1785/BSSA0770030891

Wallace, R. E. (1951). Geometry of shearing stress and relation to faulting. The Journal of Geology, 59(2), 118–130. https://doi.org/10.1086/625831

Wallach, J., Benn, K., & Rimando, R. (1995). Recent, tectonically induced, surficial stress-relief structures in the Ottawa–Hull area, Canada. Canadian Journal of Earth Sciences, 32(3), 325–333. https://doi.org/10.1139/e95-027

Walters, R. J., Elliott, J. R., D'agostino, N., England, P. C., Hunstad, I., Jackson, J. A., ... & Roberts, G. (2009). The 2009 L'Aquila earthquake (central Italy): A source mechanism and implications for seismic hazard. Geophysical Research Letters, 36(17). https://doi.org/10.1029/2009GL039337

Wang, J., Xu, C., Freymueller, J. T., Li, Z., & Shen, W. (2014). Sensitivity of Coulomb stress change to the parameters of the Coulomb failure model: A case study using the 2008 Mw 7.9 Wenchuan earthquake. Journal of Geophysical Research: Solid Earth, 119(4), 3371-3392. https://doi.org/10.1002/2012JB009860

Weeden, S. (2020). The coronavirus pandemic is pushing Canadians out of cities and into the countryside. Retrieved from https://theconversation.com/the-coronavirus-pandemic-is-pushing-canadians-out-of-cities-and-into-the-countryside-144479

Wells, D. L., & Coppersmith, K. J. (1994). New empirical relationships among magnitude, rupture length, rupture width, rupture area, and surface displacement. Bulletin of the Seismological Society of America, 84(4), 974–1002. https://doi.org/10.1785/BSSA0840040974

Wood, K. (2022). Opportunities for Rural Ontario in a Post-COVID World: A Plan for Action. Retrieved from https://www.roma.on.ca/sites/default/files/assets/DOCUMENTS/Reports/2022/OpportunitiesforRuralOntarioinaPostCOVIDWorldAPlanforActionJanuary2022FINAL.pdf

Xu, H., Xu, S., Nieto-Samaniego, Á. F., & Alaniz-Álvarez, S. A. (2017). Slicken 1.0: Program for calculating the orientation of shear on reactivated faults. Computers & Geosciences, 104, 158–165. https://doi.org/10.1016/j.cageo.2016.07.015

Yu, K., Chouinard, L. E., & Rosset, P. (2016). Seismic vulnerability assessment for Montreal. Georisk: Assessment and Management of Risk for Engineered Systems and Geohazards, 10(2), 164-178. http://dx.doi.org/10.1080/17499518.2015.1106562